



# CHORUS

This is the accepted manuscript made available via CHORUS. The article has been published as:

## Site-Selective Quantum Control in an Isotopically Enriched $^{28}\text{Si}/\text{Si}_{0.7}\text{Ge}_{0.3}$ Quadruple Quantum Dot

A.J. Sigillito, J.C. Loy, D.M. Zajac, M.J. Gullans, L.F. Edge, and J.R. Petta

Phys. Rev. Applied **11**, 061006 — Published 26 June 2019

DOI: [10.1103/PhysRevApplied.11.061006](https://doi.org/10.1103/PhysRevApplied.11.061006)

# Site-selective quantum control in an isotopically enriched $^{28}\text{Si}/\text{SiGe}$ quadruple quantum dot

A. J. Sigillito,<sup>1</sup> J. C. Loy,<sup>1</sup> D. M. Zajac,<sup>1</sup> M. J. Gullans,<sup>1</sup> L. F. Edge,<sup>2</sup> and J. R. Petta<sup>1</sup>

<sup>1</sup>*Department of Physics, Princeton University, Princeton, New Jersey 08544, USA*

<sup>2</sup>*HRL Laboratories LLC, 3011 Malibu Canyon Road, Malibu, California 90265, USA*

Silicon spin qubits are a promising quantum computing platform offering long coherence times, small device sizes, and compatibility with industry-backed device fabrication techniques. In recent years, high fidelity single-qubit and two-qubit operations have been demonstrated in Si. Here, we demonstrate coherent spin control in a quadruple quantum dot fabricated using isotopically enriched  $^{28}\text{Si}$ . We tune the ground state charge configuration of the quadruple dot down to the single electron regime and demonstrate tunable interdot tunnel couplings as large as 20 GHz, which enables exchange-based two-qubit gate operations. Site-selective single spin rotations are achieved using electric dipole spin resonance in a magnetic field gradient. We execute a resonant-CNOT gate between two adjacent spins in 270 ns.

Quantum processors based on spins in semiconductors [1–3] are rapidly becoming a strong contender in the global race to build a quantum computer. In particular, silicon is an excellent host material for spin-based quantum computing by virtue of its weak spin-orbit coupling and low natural abundance of spin-carrying nuclei, which lead to intrinsically long spin coherence times [4, 5]. Within the past few years, tremendous progress has been made in achieving high fidelity single-qubit [6, 7] and two-qubit control [8–12] in silicon. Scalable one-dimensional arrays of silicon quantum dots have been demonstrated [13], and in GaAs, where electron wavefunctions are comparably large, both one- [14–16] and two-dimensional arrays [17, 18] of spins have been fabricated. Despite this progress, quantum control of spins in silicon has been limited to one- and two-qubit devices. Scaling beyond two-qubit devices opens the door to important experiments which are currently out of reach, including error correction [19, 20], quantum simulation [21–24], and demonstrations of time crystal phases [25].

In this Letter, we demonstrate operation of a four-qubit device fabricated using an isotopically enriched  $^{28}\text{Si}/\text{SiGe}$  heterostructure. The device offers independent control of all four qubits, as well as pairwise two-qubit gates mediated by the exchange interaction [26]. We demonstrate control and measurement of the charge state of the array, and operate in the regime where each dot contains only one electron. We perform electric dipole spin resonance (EDSR) spectroscopy on all four qubits to show that they have unique spin resonance frequencies. Finally, we modulate the tunnel coupling between adjacent dots and demonstrate a resonant-CNOT gate [9, 27].

Four spin qubits are arranged in a linear array using an overlapping gate architecture, as shown in Fig. 1(a) [28]. Single spin qubits are formed by accumulating an electron under each plunger gate:  $P_1$ ,  $P_2$ ,  $P_3$ , and  $P_4$ . The couplings between dots and between dots and the charge reservoirs formed beneath gates  $S_3$  and  $D_3$  are tuned by adjusting the barrier gate voltages  $V_{B_i}$ . Charge sensing is performed by monitoring the currents  $I_{S_1}$  and

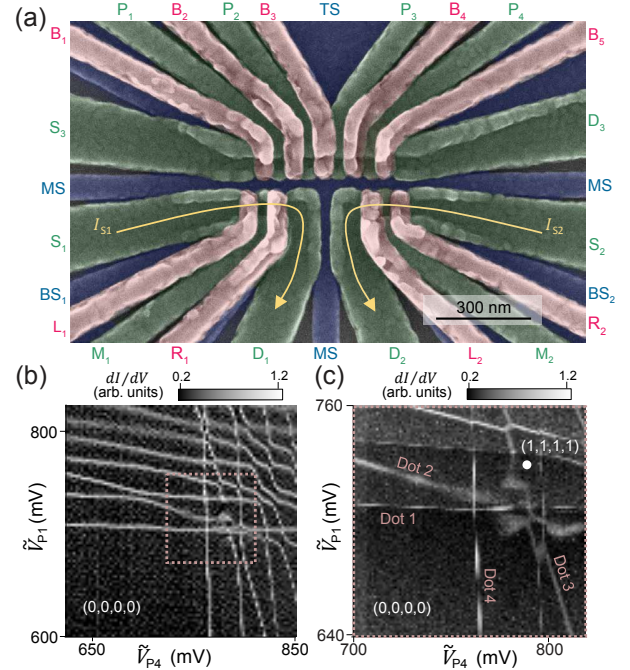


Figure 1. (a) False-color scanning electron micrograph of the device. The qubit electrons are accumulated underneath the plunger gates  $P_i$  and the charge sensor dots are formed under the gates  $M_i$ . (b) A large-scale charge stability diagram shows that the array can be emptied of electrons to reach the  $(0,0,0,0)$  charge state. The sensing signal  $dI/dV$  is obtained by combining the differentiated signal from both charge detectors. (c) Charge stability diagram acquired near the  $(1,1,1,1)$  charge state, where quantum control is performed.

$I_{S_2}$  through two proximal quantum dot charge detectors located in the lower half of the device.

Charge stability diagrams for the array are shown in Figs. 1(b-c). To obtain good charge sensitivity for all four dot charge transitions  $dI/dV = dI_{S_1}/dV_{P_1} + dI_{S_1}/dV_{P_4} + dI_{S_2}/dV_{P_1} + dI_{S_2}/dV_{P_4}$  is plotted as a function of  $V_{P_1}$  and  $V_{P_4}$ . In Fig. 1(b) we show that we can achieve the  $(N_1, N_2, N_3, N_4) = (0, 0, 0, 0)$  charge state, where  $N_i$  denotes the number of electrons in dot  $i$ . The  $(0, 0, 0, 0)$

charge state is evident from the large region devoid of charge transitions in the lower left corner of the figure. The device is typically operated in the (1,1,1,1) charge state, which is labeled in the zoomed-in charge stability diagram of Fig. 1(c). The capacitive coupling between plunger gates and neighboring dots (i.e. gate  $P_1$  and dot 2) is naturally an order of magnitude weaker than the coupling between a plunger gate and the dot formed directly underneath it (i.e. gate  $P_1$  and dot 1) [28]. It can therefore be challenging to distinguish charge transitions in adjacent dots ( $P_1$  and  $P_2$ , or  $P_3$  and  $P_4$ ) in two-dimensional charge stability plots since the slopes are very similar. To more clearly distinguish the charge transitions, an artificial cross-coupling was added between each plunger gate and its neighboring plunger gates in software (details available in the supplementary information [29]) such that a sweep in  $V_{P_1}$  and  $V_{P_4}$  not only induces transitions in dots 1 and 4, but also in dots 2 and 3. To distinguish when the artificial coupling is used, we relabel  $V_{P_1}$  and  $V_{P_4}$  as  $\tilde{V}_{P_1}$  and  $\tilde{V}_{P_4}$ , respectively. With the (1,1,1,1) charge state having been identified, we next establish virtual gates, which significantly streamline device tuning.

Virtual gates have been described in detail and compensate for the effects of device cross-capacitance through software corrections that effectively invert the capacitance matrix [21, 30–33]. Whenever the voltage of gate  $V_{P_i}$  is adjusted to tune the chemical potential of dot  $i$ , the voltages on adjacent gates  $V_{P_{(i-1)}}$  and  $V_{P_{(i+1)}}$  are modified by a calibrated amount to keep the chemical potentials of dots  $i-1$  and  $i+1$  constant. The measured capacitance matrix is given in the supplementary information [29] and is used to establish the virtual gate space [30].

Pairwise charge stability diagrams measured using virtual gates are shown in Figs. 2(a–c). As the two virtual gates  $u_i$  and  $u_{i+1}$  are swept, the charge sensor currents  $I_{S1}$  and  $I_{S2}$  are measured. Here we plot  $I_{S1} - I_{S2}$  as it results in higher charge sensing contrast. Gates not being swept [i.e.  $u_3$  and  $u_4$  in Fig. 2(a)] are held fixed at the same chemical potential as the source and drain reservoirs to enable fast loading and unloading of electrons throughout the array. The orthogonality of the charge transitions indicates that we have independent control of each quantum dot’s chemical potential.

Loss & DiVincenzo suggested that the exchange interaction between two spins could be modulated by adjusting the height of the tunnel barrier separating the spins [1]. We demonstrate control over all of the interdot tunnel couplings ( $t_{cij}$ ) in our device by measuring the charge state occupation as a function of detuning  $\epsilon_{ij}$  for different barrier gate voltages  $V_{Bi}$ . Figure 2(d) plots  $P_{(0,1,*,*)}$  along the detuning axis shown in Fig. 2(a). The \* denotes that the chemical potential of the dot is held at the same value as the source and drain chemical potentials. As the tunnel coupling is increased, the charge delocalizes across adjacent dots and the interdot charge transition broadens. These data are fit as described in [34, 35] to

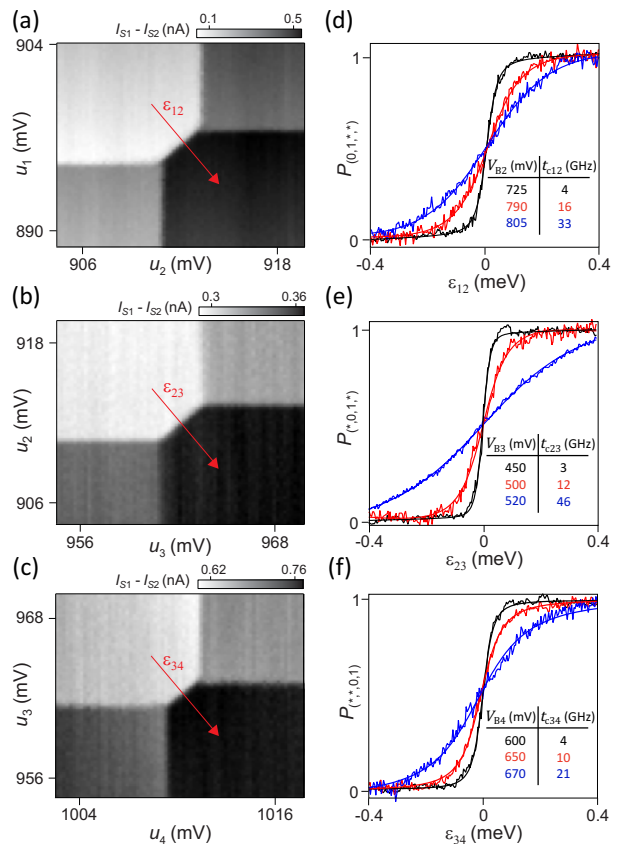


Figure 2. Pairwise charge stability diagrams measured for (a) dots 1 and 2, (b) dots 2 and 3, and (c) dots 3 and 4. Here we use virtual gates to independently tune each dot’s chemical potential. (d–f) Charge state occupation measured as a function of detuning  $\epsilon_{ij}$  for various barrier gate voltages  $V_{Bi}$ . An increase in interdot tunnel coupling broadens the interdot charge transitions. The data are fit to theory (solid lines) to extract the interdot tunnel coupling  $t_{cij}$  between dots  $i$  and  $j$  [34].

extract the interdot tunnel coupling. The lever arm conversion between gate voltage and energy is determined by measuring finite bias triangles for each pair of dots as reported in Table 1. As shown in the data, the device offers a high degree of control, with tunnel coupling tunable from  $2t_{cij} \approx k_B T_e \approx 2$  GHz to many 10’s of GHz, which is sufficient to enable fast CNOT gates. Here  $k_B$  is Boltzmann’s constant and the electron temperature  $T_e \approx 90$  mK is obtained by fitting the charge transitions to the source and drain to a Fermi function as described in [13].

Site-selective single spin rotations are achieved using EDSR [36, 37] in the presence of a magnetic field gradient generated by a Co micromagnet [29]. The field from the micromagnet  $B_i^M$  is different at each dot and therefore each spin has a unique electron spin resonance frequency  $f_i$  given by  $hf_i = g\mu_B(B_{ext} + B_i^M)$ , where  $h$  is Planck’s constant,  $g \approx 2$  is the Landé g factor, and  $B_{ext}$  is the externally applied magnetic field. Our micromagnet design is similar to that used by Yoneda *et al.* [38], but it has a

Dot	$\alpha$ (meV/mV)	$E_c$ (meV)	$B_i^M$ (mT)	$T_2^*$ ( $\mu$ s)	$T_{2,echo}$ ( $\mu$ s)
1	0.14	4.5	137.6	2.6	41
2	0.13	4.7	165.8	1.5	31
3	0.14	4.5	194.3	10.4	72
4	0.15	4.7	199.2	9.4	109

Table I. Summary of single-qubit parameters including lever-arm conversion between gate voltage and energy  $\alpha$ , charging energy  $E_c$ , magnetic field offset due to the micromagnet  $B_i^M$ , spin dephasing time  $T_2^*$ , and spin coherence time  $T_{2,echo}$ .

slanting edge (as seen from above) that extends the field gradient over the entire quadruple quantum dot [29].

To map out  $B_i^M$ , EDSR spectroscopy is performed on each qubit. During spectroscopy, the array is configured such that only dot  $i$  contains a single electron – all other dots are empty. In practice, we find that adding an electron to an adjacent dot only shifts the resonance frequency by a few MHz. A frequency chirped microwave pulse ( $\pm 15$  MHz around a frequency  $f$  for 120  $\mu$ s) is applied to gate MS. If the chirped pulse sweeps through the spin resonance frequency  $f_i$  of dot  $i$ , its spin will end up in a mixed state. Here our chirped pulses are not adiabatic, but are nonetheless convenient for identifying spin resonance conditions, as the linewidth of electron spins in  $^{28}\text{Si}$  can be narrow ( $< 100$  kHz). The spin state of dot  $i$  is then measured through spin-selective tunneling to the leads [39]. In the case of  $i = 2$  and  $i = 3$ , where the dots are not directly connected to the leads, the electron is shuttled to the edge of the array and read out in dots 1 or 4, respectively. Loading the array follows the read out sequence in reverse. These measurements are repeated over a range of  $B_{ext}$  spanning 250 – 450 mT.

The spectra for all four qubits are summed and plotted in Fig. 3(a). The field gradient from the micromagnet separates the qubit resonance frequencies by hundreds of MHz, as highlighted by the linecut through the data in Fig. 3(b). For comparison, in silicon devices relying on Stark shifts or interface disorder for spin selectivity, the qubit splitting is typically a few 10's of MHz [8, 11]. We find that over the course of  $\sim 24$  hours the qubit frequencies are constant to within a few hundred kilohertz. The readout visibility is primarily limited by  $T_e$  and spin relaxation ( $T_1 = 52$  ms for qubit 4). The latter can be overcome by employing cryogenic current amplifiers to reduce noise and improve the measurement bandwidth [40].

We next measure the spin dephasing times  $T_2^*$  and spin coherence times  $T_2$  for each qubit (see Table 1). In natural silicon, spin coherence is limited by the hyperfine interaction with the 4.7% abundant  $^{29}\text{Si}$  nuclei. Here, our device consists of an isotopically enriched  $^{28}\text{Si}$  quantum well, which is 4.9 nm thick and has only an 800 ppm residual concentration of  $^{29}\text{Si}$  [41, 42]. The buffer layers, however, consist of  $^{nat}\text{Si}$  and  $^{nat}\text{Ge}$  containing residual spin-1/2 and spin-9/2 nuclei, respectively. Wavefunction

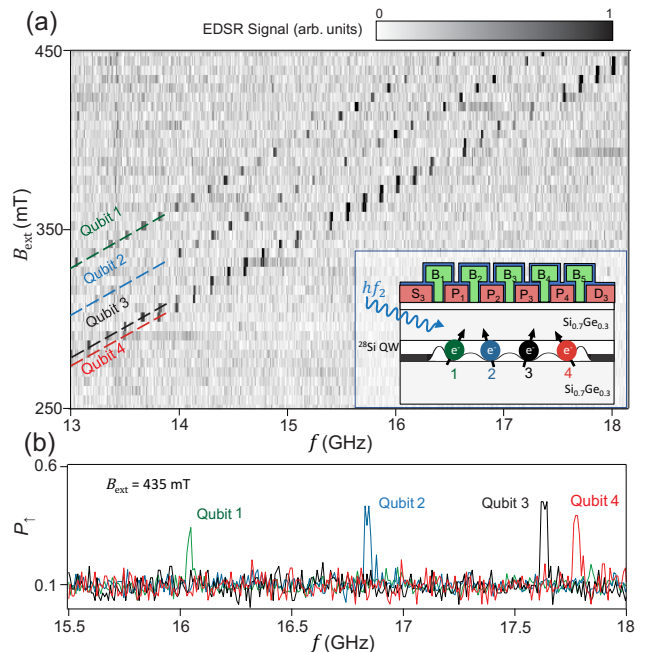


Figure 3. (a) Summed EDSR spectra for all four qubits. The qubits are driven using gate MS and four distinct ESR transitions are observed. The ESR lines do not appear continuous due to undersampling in  $B_{ext}$ . Inset: Cross-sectional cartoon of the device showing all four qubits subject to the same driving field, but with only qubit 2 on resonance. (b) A line cut through the data at  $B_{ext} = 435$  mT shows that all four qubits are well separated in frequency. The spacing between qubits 1, 2, and 3 is  $\sim 800$  MHz and qubits 3 and 4 are separated by  $\sim 130$  MHz. The qubit linewidths are broadened by the 30 MHz microwave chirp used in these measurements.

overlap with these nuclei will be non-negligible given the relatively thin quantum well [43].

$T_2^*$  is determined through measurements of Ramsey fringes. For each Ramsey decay curve, the data are integrated over 15 minutes. Qubits 3 and 4 show a nearly tenfold increase in  $T_2^*$  compared with  $T_2^* \sim 1$   $\mu$ s for electron spins in natural silicon, whereas qubits 1 and 2 have a dephasing time that is comparable to natural silicon. A simple Hahn echo pulse sequence significantly extends the coherence times, as summarized in Table 1. Similar fluctuations in the coherence times have been observed in other devices [9–11] and may be due to sampling over a relatively small number of spin-carrying nuclei in the quantum well and SiGe barrier layers. Another reason for the fast dephasing in qubits 1 and 2 could be charge noise which has been shown to shorten  $T_1$  [44] and  $T_2$  [6] in the presence of field gradients and is discussed in the supplementary information [29]. Due to the wedge shaped geometry of the micromagnet, the field gradient experienced by qubits 1 and 2 is significantly larger than at sites 3 and 4 which is evident from the large change in field offsets  $B_i^M$  between dots 1-3, and a relatively small change in  $B_i^M$  between dots 3 and 4 (see Table 1). The short coherence times in dots 1 and 2 are still comparable with the times reported in natural Si/SiGe and are not

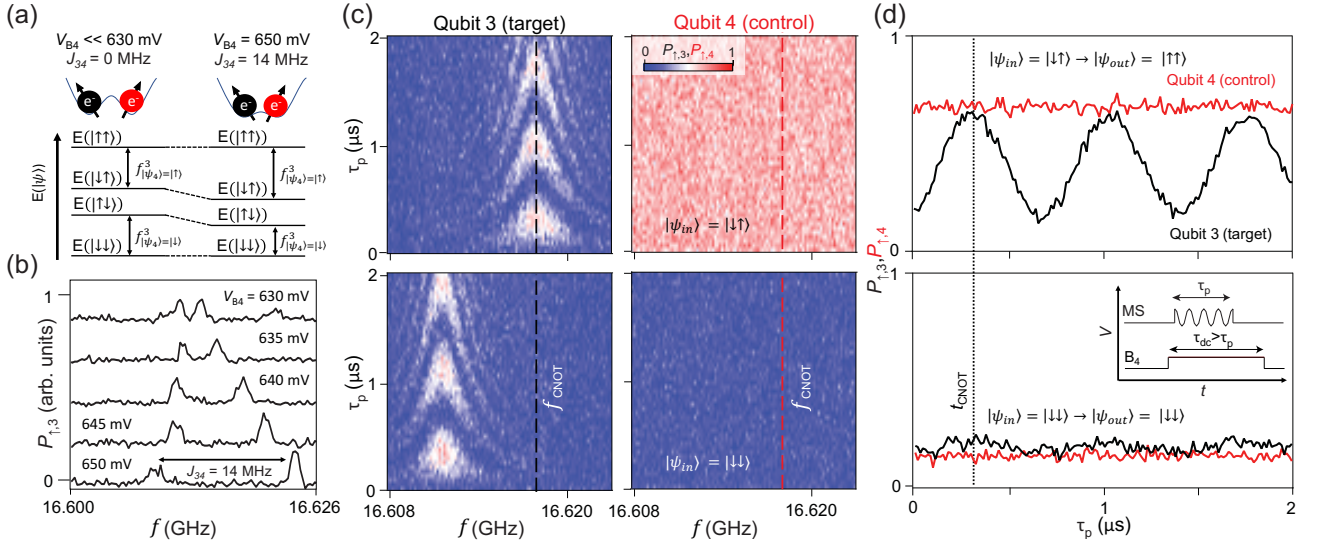


Figure 4. (a) Energy level diagram for dots 3 and 4 subject to a magnetic field gradient and either no exchange (left) or finite exchange (right). Increasing  $V_{B4}$  turns on the exchange interaction  $J_{34}$  between qubits 3 and 4. Under exchange, the spin transition frequency of qubit 3 (the target qubit)  $f^{(3)}$  depends on the input state of qubit 4  $|\Psi_4\rangle$  (the control qubit). (b) EDSR spectroscopy of qubit 3. The spin-up probability  $P_{\uparrow,3}$  is plotted as a function of  $f$  and  $V_{B4}$ . (c) By varying the frequency and amplitude of a microwave pulse applied to the target qubit with the control qubit prepared in either the up state (top panels) or the down state (bottom panels), we map out the frequency of the target qubit conditioned on the state of the control qubit. (d) Driving at frequency  $f_{\text{CNOT}}$  and varying the microwave burst time  $\tau_p$  results in Rabi oscillations of the target qubit that are conditioned on the state of the control qubit. When the microwave burst is timed to correspond to a  $\pi$ -rotation on the target qubit,  $\tau_p = \tau_{\text{CNOT}} = 270$  ns, a CNOT gate is achieved (dotted line).

prohibitive for two-qubit operation.

Two-qubit gates are performed by applying voltage pulses to the barrier gates  $B_i$  separating the dots [1]. Applying a positive voltage to a barrier gate increases wavefunction overlap between adjacent dots and turns on exchange [27], as illustrated in the energy level diagram of Fig. 4(a). To first map out the influence of the barrier gate on the exchange interaction, we vary the gate voltage  $V_{B4}$  and perform EDSR spectroscopy on qubit 3, as shown in Fig. 4(b). Before measuring the EDSR spectrum of qubit 3, qubit 4 was prepared in a mixed state such that any state dependent line splitting could be observed [9]. The EDSR spectrum of qubit 4 is probed in a similar way. As  $V_{B4}$  is increased, the EDSR lines split to reveal a doublet with a peak separation that is equal to the exchange energy  $J_{34}$ . The overall frequency shift of the doublet is attributed to the displacement of the electron's wavefunction within the magnetic field gradient as  $V_{B4}$  is adjusted [9]. When applying voltage pulses to any gates, these induced frequency shifts must be accounted for and corrected using single qubit  $z$ -rotations [9, 45].

A resonant-CNOT gate can be achieved using this device architecture by following the protocol developed by Zajac *et al.* [9]. Here we focus on qubits 3 and 4, while dots 1 and 2 are empty. With  $J_{34} \approx 0$ , we prepare input state  $|\psi_{in}\rangle = |\downarrow\downarrow\rangle$  through spin-selective tunneling or input state  $|\psi_{in}\rangle = |\downarrow\uparrow\rangle$  through spin-selective tunneling followed by a  $\pi$ -pulse on spin 4. We then apply a voltage pulse to gate  $B_4$  to turn on exchange while simultaneously applying a microwave burst of varying duration

$\tau_p$  and frequency  $f$ . The resulting spin-up probabilities  $P_{\uparrow,3}(P_{\uparrow,4})$  for qubit 3(4) are plotted in Fig. 4(c). Rabi oscillations are observed for qubit 3 with a resonance frequency that is dependent on the state of qubit 4. By setting  $f = f_{\text{CNOT}}$ , where the microwave tone is resonant with the target qubit when the control qubit is in the spin-up state, we drive Rabi oscillations on the target qubit conditioned on the state of the control qubit [see Fig. 4(d)]. Furthermore, when  $t = t_{\text{CNOT}}$ , qubit 3 will be flipped when qubit 4 is in the spin-up state. With these settings, we realize a resonant-CNOT gate in a four qubit device [9, 27]. To implement a high fidelity CNOT gate, it is important to note that some additional phase accumulation due to the  $V_{B4}$ -induced Ising interaction must be compensated for by properly tuning  $\tau_{\text{DC}}$  and  $V_{B4}$  as described in our previous work [9, 27]. We attribute the slight oscillations that appear on qubit 3 in the lower panel of Fig. 4(d) to state preparation errors on qubit 4. Off-resonant driving would lead to oscillations at a frequency above 6 MHz.

In conclusion, we have demonstrated one- and two-qubit gate operations in a four qubit device fabricated from an isotopically enriched  $^{28}\text{Si}$  quantum well. Our device design allows for full control of the charge state in the array. Interdot tunnel coupling and exchange are tuned using barrier gates. We demonstrate independent control of all four qubits, which is enabled by the field gradient from a Co micromagnet. To demonstrate a two-qubit gate involving dots 3 and 4, we mapped exchange as a function of  $V_{B4}$  and performed a resonant-CNOT gate

in 270 ns. These results set the stage for a four qubit spin-based quantum processor in silicon, which should be capable of performing small-scale quantum algorithms and demonstrating time crystal phases [25].

Funded by Army Research Office grant No. W911NF-15-1-0149, DARPA grant No. D18AC0025, and the Gordon and Betty Moore Foundation's EPIQS Initiative

through Grant GBMF4535. Devices were fabricated in the Princeton University Quantum Device Nanofabrication Laboratory. The authors acknowledge the use of Princetons Imaging and Analysis Center, which is partially supported by the Princeton Center for Complex Materials, a National Science Foundation (NSF)-MRSEC program (DMR-1420541).

- 
- [1] D. Loss and D. P. DiVincenzo, Quantum computation with quantum dots, *Phys. Rev. A* **57**, 120 (1998).
- [2] R. Hanson, L. P. Kouwenhoven, J. R. Petta, S. Tarucha, and L. M. K. Vandersypen, Spins in few-electron quantum dots, *Rev. Mod. Phys.* **79**, 1217 (2007).
- [3] F. A. Zwanenburg, A. S. Dzurak, A. Morello, M. Y. Simmons, L. C. L. Hollenberg, G. Klimeck, S. Rogge, S. N. Coppersmith, and M. A. Eriksson, Silicon quantum electronics, *Rev. Mod. Phys.* **85**, 961 (2013).
- [4] A. M. Tyryshkin, S. Tojo, J. J. L. Morton, H. Riemann, N. V. Abrosimov, P. Becker, H.-J. Pohl, T. Schenkel, M. L. W. Thewalt, K. M. Itoh, and S. A. Lyon, Electron spin coherence exceeding seconds in high-purity silicon, *Nat. Mater.* **11**, 143 (2012).
- [5] M. Veldhorst, J. C. C. Hwang, C. H. Yang, A. W. Leenstra, B. De Ronde, J. P. Dehollain, J. T. Muhonen, F. E. Hudson, K. M. Itoh, A. Morello, and A. S. Dzurak, An addressable quantum dot qubit with fault-tolerant control-fidelity, *Nat. Nanotechnol.* **9**, 981 (2014).
- [6] J. Yoneda, K. Takeda, T. Otsuka, T. Nakajima, M. R. Delbecq, G. Allison, T. Honda, T. Kodera, S. Oda, Y. Hoshi, N. Usami, K. M. Itoh, and S. Tarucha, A quantum-dot spin qubit with coherence limited by charge noise and fidelity higher than 99.9%, *Nat. Nanotechnol.* **13**, 102 (2018).
- [7] C. H. Yang, K. W. Chan, R. Harper, W. Huang, T. Evans, J. C. C. Hwang, B. Hensen, A. Laucht, T. Tanttu, F. E. Hudson, S. T. Flammia, K. M. Itoh, A. Morello, S. D. Bartlett, and A. S. Dzurak, Silicon qubit fidelities approaching incoherent noise limits via pulse optimisation, *Nat. Electron.* **2**, 151 (2019).
- [8] M. Veldhorst, C. H. Yang, J. C. C. Hwang, W. Huang, J. P. Dehollain, J. T. Muhonen, S. Simmons, A. Laucht, F. E. Hudson, K. M. Itoh, A. Morello, and A. S. Dzurak, A two-qubit logic gate in silicon, *Nature* **526**, 410 (2015).
- [9] D. M. Zajac, A. J. Sigillito, M. Russ, F. Borjans, J. M. Taylor, G. Burkard, and J. R. Petta, Resonantly driven CNOT gate for electron spins, *Science* **359**, 439 (2018).
- [10] T. F. Watson, S. G. J. Philips, E. Kawakami, D. R. Ward, P. Scarlino, M. Veldhorst, D. E. Savage, M. G. Lagally, M. Friesen, S. N. Coppersmith, M. A. Eriksson, and L. M. K. Vandersypen, A programmable two-qubit quantum processor in silicon, *Nature* **555**, 633 (2018).
- [11] W. Huang, C. H. Yang, K. W. Chan, T. Tanttu, B. Hensen, R. C. C. Leon, M. A. Fogarty, J. C. C. Hwang, F. E. Hudson, K. M. Itoh, A. Morello, A. Laucht, and A. S. Dzurak, Fidelity benchmarks for two-qubit gates in silicon, arXiv:1805.05027.
- [12] X. Xue, T. F. Watson, J. Helsen, D. R. Ward, D. E. Savage, M. G. Lagally, S. N. Coppersmith, M. A. Eriksson, S. Wehner, and L. M. K. Vandersypen, Benchmarking Gate Fidelities in a Si/SiGe Two-Qubit Device, *Phys. Rev. X* **9**, 021011 (2019).
- [13] D. M. Zajac, T. M. Hazard, X. Mi, E. Nielsen, and J. R. Petta, Scalable gate architecture for a one-dimensional array of semiconductor spin qubits, *Phys. Rev. Appl.* **6**, 054013 (2016).
- [14] A. Noiri, J. Yoneda, T. Nakajima, T. Otsuka, M. R. Delbecq, K. Takeda, S. Amaha, G. Allison, A. Ludwig, A. D. Wieck, and S. Tarucha, Coherent electron-spin-resonance manipulation of three individual spins in a triple quantum dot, *Appl. Phys. Lett.* **108**, 153101 (2016).
- [15] T. Otsuka, T. Nakajima, M. R. Delbecq, S. Amaha, J. Yoneda, K. Takeda, G. Allison, T. Ito, R. Sugawara, A. Noiri, A. Ludwig, A. D. Wieck, and S. Tarucha, Single-electron spin resonance in a quadruple quantum dot, *Sci. Rep.* **6**, 31820 (2016).
- [16] T. Ito, T. Otsuka, T. Nakajima, M. R. Delbecq, S. Amaha, J. Yoneda, K. Takeda, A. Noiri, G. Allison, A. Ludwig, A. D. Wieck, and S. Tarucha, Four single-spin Rabi oscillations in a quadruple quantum dot, *Appl. Phys. Lett.* **113**, 093102 (2018).
- [17] P.-A. Mortemousque, E. Chanrion, B. Jadot, H. Flentje, A. Ludwig, A. D. Wieck, M. Urdampilleta, C. Bauerle, and T. Meunier, Coherent control of individual electron spins in a two dimensional array of quantum dots, arXiv:1808.06180 (2018).
- [18] U. Mukhopadhyay, J. P. Dehollain, C. Reichl, W. Wegscheider, and L. M. K. Vandersypen, A 2x2 quantum dot array with controllable inter-dot tunnel couplings, *Appl. Phys. Lett.* **112**, 183505 (2018).
- [19] M. D. Reed, L. DiCarlo, S. E. Nigg, L. Sun, L. Frunzio, S. M. Girvin, and R. J. Schoelkopf, Realization of three-qubit quantum error correction with superconducting circuits, *Nature* **482**, 382 (2012).
- [20] P. Schindler, J. T. Barreiro, T. Monz, V. Nebendahl, D. Nigg, M. Chwalla, M. Hennrich, and R. Blatt, Experimental repetitive quantum error correction, *Science* **332**, 1059 (2011).
- [21] T. Hensgens, T. Fujita, L. Janssen, X. Li, C. J. van Diepen, C. Reichl, W. Wegscheider, S. Das Sarma, and L. M. K. Vandersypen, Quantum simulation of a Fermi-Hubbard model using a semiconductor quantum dot array, *Nature* **548**, 70 (2017).
- [22] I. M. Georgescu, S. Ashhab, and F. Nori, Quantum simulation, *Rev. Mod. Phys.* **86**, 153 (2014).
- [23] P. Barthélemy and L. M. K. Vandersypen, Quantum dot systems: a versatile platform for quantum simulations, *Ann. Phys.* **525**, 808 (2013).
- [24] T. Byrnes, N. Y. Kim, K. Kusudo, and Y. Yamamoto, Quantum simulation of Fermi-Hubbard models in semiconductor quantum-dot arrays, *Phys. Rev. B* **78**, 075320 (2008).
- [25] E. Barnes, J. M. Nichol, and S. E. Economou, Stabiliza-

- tion and manipulation of multispin states in quantum-dot time crystals with Heisenberg interactions, *Phys. Rev. B* **99**, 035311 (2019).
- [26] J. R. Petta, A. C. Johnson, J. M. Taylor, E. A. Laird, A. Yacoby, M. D. Lukin, C. M. Marcus, M. P. Hanson, and A. C. Gossard, Coherent manipulation of coupled electron spins in semiconductor quantum dots, *Science* **309**, 2180 (2005).
- [27] M. Russ, D. M. Zajac, A. J. Sigillito, F. Borjans, J. M. Taylor, J. R. Petta, and G. Burkard, High-fidelity quantum gates in Si/SiGe double quantum dots, *Phys. Rev. B* **97**, 085421 (2018).
- [28] D. M. Zajac, T. M. Hazard, X. Mi, K. Wang, and J. R. Petta, A reconfigurable gate architecture for Si/SiGe quantum dots, *Appl. Phys. Lett.* **106**, 223507 (2015).
- [29] See Supplemental Material at [URL will be inserted by publisher] for additional device characterization data including references [6,13,30,38,43-45].
- [30] A. R. Mills, D. M. Zajac, M. J. Gullans, F. J. Schupp, T. M. Hazard, and J. R. Petta, Shuttling a single charge across a one-dimensional array of silicon quantum dots, *Nat. Commun.* **10**, 1063 (2019).
- [31] T. A. Baart, M. Shafiei, T. Fujita, C. Reichl, W. Wegscheider, and L. M. K. Vandersypen, Single-spin CCD, *Nat. Nanotechnol.* **11**, 330 (2016).
- [32] C. J. van Diepen, P. T. Eendebak, B. T. Buijtdorp, U. Mukhopadhyay, T. Fujita, C. Reichl, W. Wegscheider, and L. M. K. Vandersypen, Automated tuning of interdot tunnel coupling in double quantum dots, *Appl. Phys. Lett.* **113**, 033101 (2018).
- [33] C. Volk, A. M. J. Zwerver, U. Mukhopadhyay, P. T. Eendebak, C. J. van Diepen, J. P. Dehollain, T. Hensgens, T. Fujita, C. Reichl, W. Wegscheider, and L. M. K. Vandersypen, Loading a quantum-dot based “qubyte” register, *npj Quantum Inf.* **5**, 29 (2019).
- [34] L. DiCarlo, H. J. Lynch, A. C. Johnson, L. I. Childress, K. Crockett, C. M. Marcus, M. P. Hanson, and A. C. Gossard, Differential charge sensing and charge delocalization in a tunable double quantum dot, *Phys. Rev. Lett.* **92**, 226801 (2004).
- [35] J. R. Petta, A. C. Johnson, C. M. Marcus, M. P. Hanson, and A. C. Gossard, Manipulation of a single charge in a double quantum dot, *Phys. Rev. Lett.* **93**, 186802 (2004).
- [36] M. Pioro-Ladriere, T. Obata, Y. Tokura, Y.-S. Shin, T. Kubo, K. Yoshida, T. Taniyama, and S. Tarucha, Electrically driven single-electron spin resonance in a slanting Zeeman field, *Nat. Phys.* **4**, 776 (2008).
- [37] Y. Tokura, W. G. van der Wiel, T. Obata, and S. Tarucha, Coherent single electron spin control in a slanting Zeeman field, *Phys. Rev. Lett.* **96**, 047202 (2006).
- [38] J. Yoneda, T. Otsuka, T. Takakura, M. Pioro-Ladrière, R. Brunner, H. Lu, T. Nakajima, T. Obata, A. Noiri, C. J. Palmstrøm, A. C. Gossard, and S. Tarucha, Robust micromagnet design for fast electrical manipulations of single spins in quantum dots, *APEX* **8**, 084401 (2015).
- [39] J. M. Elzerman, R. Hanson, L. H. W. Van Beveren, B. Witkamp, L. M. K. Vandersypen, and L. P. Kouwenhoven, Single-shot read-out of an individual electron spin in a quantum dot, *Nature* **430**, 431 (2004).
- [40] I. T. Vink, T. Nooitgedagt, R. N. Schouten, L. M. K. Vandersypen, and W. Wegscheider, Cryogenic amplifier for fast real-time detection of single-electron tunneling, *Appl. Phys. Lett.* **91**, 123512 (2007).
- [41] P. W. Deelman, L. F. Edge, and C. A. Jackson, Metamorphic materials for quantum computing, *Mater. Res. Bull.* **41**, 224 (2016).
- [42] C. J. K. Richardson, C. A. Jackson, L. F. Edge, and P. W. Deelman, High-resolution x-ray reflection Fourier analysis of metamorphic Si/SiGe quantum wells, *J. Vac. Sci. Technol. B* **35**, 02B113 (2017).
- [43] W. M. Witzel, M. S. Carroll, L. Cywiński, and S. Das Sarma, Quantum decoherence of the central spin in a sparse system of dipolar coupled spins, *Phys. Rev. B* **86**, 035452 (2012).
- [44] F. Borjans, D. Zajac, T. Hazard, and J. Petta, Single-spin relaxation in a synthetic spin-orbit field, *Phys. Rev. Appl.* **11**, 044063 (2019).
- [45] K. Takeda, J. Yoneda, T. Otsuka, T. Nakajima, M. Delbecq, G. Allison, Y. Hoshi, N. Usami, K. Itoh, S. Oda, T. Kodera, and S. Tarucha, Optimized electrical control of a Si/SiGe spin qubit in the presence of an induced frequency shift, *npj Quantum Inf.* **4**, 54 (2018).